

## Fiscal Year 2000 Annual Summary Report

### Methods for Design and Interrogation of FGM Objects

---

#### Principal/co-Principal Investigator.

- \* PI/co-PI Name(s): Nicholas M. Patrikalakis, Emanuel M. Sachs
  - \* PI Institution: Massachusetts Institute of Technology
  - \* PI Phone Number: (617)253-4555
  - \* PI Fax Number: (617)253-8125
  - \* PI E-mail Address: [nmp@mit.edu](mailto:nmp@mit.edu), [sachs@mit.edu](mailto:sachs@mit.edu)
  - \* PI URL Home Page: <http://www.mit.edu/~tdp>, <http://deslab.mit.edu/3dp>
  - \* Grant/Contract Number: N00014-00-1-0169
  - \* Period of Performance: 01/01/00 - 09/15/00
- 

#### Project Attributes.

- \* Number of refereed papers/book chapters published: 1
  - \* Number of refereed papers/book chapters to appear: 1
  - \* Number of books published: 0
  
  - \* Number of unrefereed reports and other articles: 3
  - \* Number of project presentations: 4
  
  - \* Number of patents granted and software copyrights: 1
  - \* Number of patents filed but not yet granted: 0
  
  - \* Number of graduate students supported  $\geq$  25% of full time: 0
  - \* Number of post-docs supported  $\geq$  25% of full time: 1
  - \* Number of minorities supported: 0
- 

#### Summary of Objectives and Approach.

One of the great potential benefits offered by solid freeform fabrication (SFF) technology is the ability to create parts that have composition variation within them. Such local composition control (LCC) has the potential to create new classes of components. For example, monolithic components can be created, which integrate the function of multiple discrete components. Alternatively, material composition can be tailored within a component to achieve local control of properties (e.g., hardness vs. toughness, magnetic properties, corrosion properties, etc.). The objective of this project is to develop algorithms for the design of objects with functionally graded material (FGM) composition or alternatively of objects with local composition control (LCC) and their interrogation for visualization, and fabrication through post-processing including volume dithering and encoding, and 3D Printing (3DP).

---

## Summary of Technical Progress.

### - Information Flow:

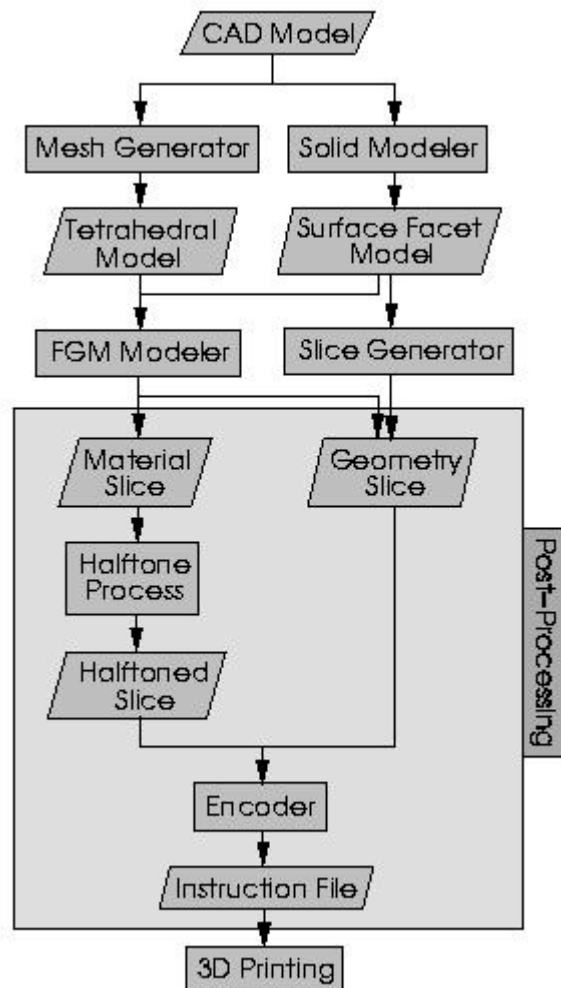


Figure 1: One-way information flow for LCC with 3D Printing

The current information flow [CHO-00,HW00] for local composition control (LCC) with 3D Printing is composed of four major steps: geometric design, material design, post-processing, and fabrication. This information pathway establishes a clear separation between design of FGM objects, their processing, and their fabrication. The geometric information is exported from the CAD system as a standard exchange format such as IGES, followed by the generation of tetrahedral meshes. The internal composition will be established by prescribing/interpolating the composition of the vertices of each tetrahedron. The post-processing converts the designed FGM model into machine instructions. To fill the gap between the design and fabrication stages, the post-processing slices the FGM model to generate layer-wise information, and transforms the continuous-tone material composition into printable, discrete information through halftoning (or dithering) process. By merging the halftoned material information with the sliced geometric information<sup>1</sup> through printing patterns, we generate machine instructions that control the 3D printer. Figure 1 illustrates the information pathway.

---

<sup>1</sup> Geometric slice can be generated by slicing either tetrahedral model or surface facet model (.STL) as shown in Figure 1, and a result with finer resolution is used.

#### - Demonstration of Complete Pathway:

In order to test and demonstrate the complete information and 3D printing pathway, a part of representative complexity was chosen. The solid model of this prototypical molding tool is shown in Figure 2-(a). The model was created in ProEngineer and exported both as IGES and .STL files.

The IGES file was imported to Algor (a commercial finite-element analysis package) and was used to create a tetrahedral mesh<sup>3</sup>.

Simulating the use of material control to locally control the hardness of the surface of the tool, a composition profile of materials **A** and **B** was designed. Linear grading normal to the surface was used as illustrated in Figure 2-(a) with the constraint that the sum of the compositions was 100% at all locations. This composition profile was imposed on the 3D mesh by computing the minimum distance from each node to the boundary. A material slice was then created using interpolation between 3D nodes to define compositions at the FGM triangles defined by the slicing. The material slices were then subjected to a 2D halftoning algorithm using a dither cell which was 8 PELs along the fast axis and 4 PELs perpendicular to it. The PELs are rectangular with a size along the fast axis of  $30\mu m$  and  $202\mu m$  perpendicular to it. Thus the dither cell was  $240\mu m$  along the fast axis and  $808\mu m$  perpendicular to it. The  $8 \times 4$  dither cell allows for the definition of 33 levels of composition for each material. Figure 2-(b) shows a halftoned material slice (slice #81 - about half-way up the part) where magenta is used to represent material **A** and cyan is used to represent material **B**. Without special consideration, the absence of material specification outside the geometric boundary of the part would lower the material density specified by dither cells which intersect the boundary, as the value for the dither cell is determined by averaging over the entire dither cell. To correct for this, all PELs were pre-initialized to material **A** and then over-written by the composition determined from the material slice.

The .STL file exported from ProEngineer was used to model the boundary of the part and geometry slices such as that shown in Figure 2-(c) where derived from it.

The reconciliation of the material and geometric slices in Figures 2-(b,c), is part of the encoding process that produces the instructions for the 3D Printing machine. Figure 2-(d) shows a photograph of layer #81 as printed on the machine. Note the reasonable correspondence between printed layer and the expected result.

---

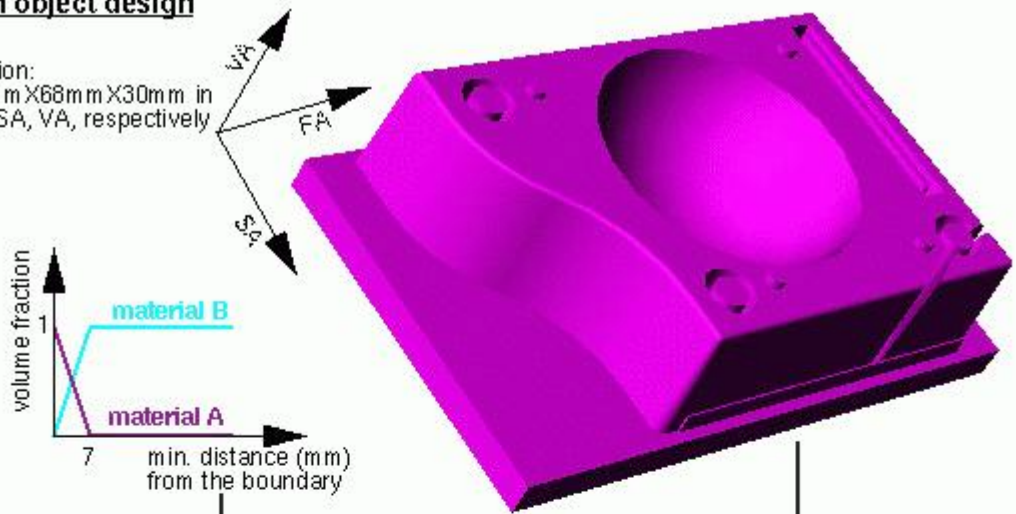
<sup>3</sup> The boundary of the solid was tessellated with a normalized/non-dimensional mesh resolution ( $\approx 2 \times 10^{-2}$ ), and a 3D mesh composed of 290,234 tetrahedra was generated from the tessellated boundary front.

#### - Alternative Representations and Evaluations:

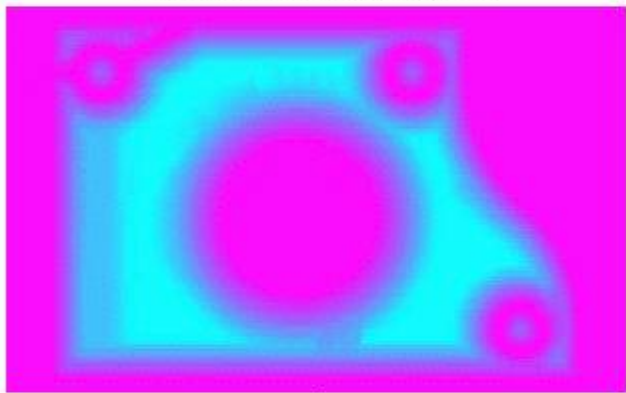
We have analyzed various data structures for representing FGM objects including a voxel-based structure, finite-element mesh approach, and the generalized boundary representation (B-rep) data

**(a) FGM object design**

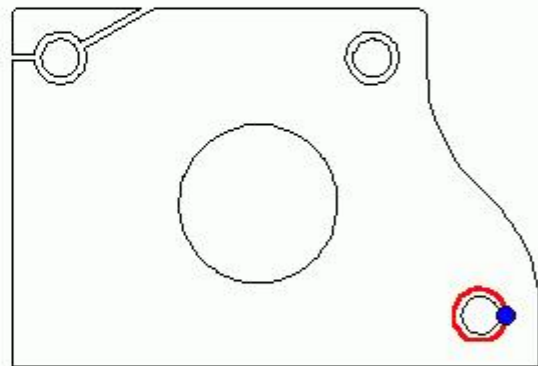
Dimension:  
- 110mm X68mm X30mm in  
FA, SA, VA, respectively



**(b) halftoned material slice**



**(c) geometric slice**



**(d) printed layer**

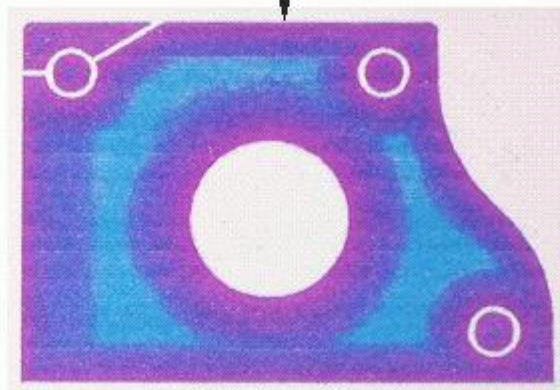


Figure 2: Implementation: functionally graded two-material object

structures in order to represent spatially varying geometric/material properties [TRJ00]. A voxel-based modeling is an exhaustive enumeration approach, where a region of space containing the object is decomposed into a lattice of voxels and a vector of numerical values are associated with each voxel for blended compositions. In the finite-element mesh approach, material or physical property fields are attached to the nodes in the mesh. Interpolation functions (e.g., linear) associated with the volume elements (e.g., linear tetrahedra) are used to define the composition throughout each element as functions of the values assigned to the nodes. Generalized B-Rep data structure maintains the topology of a model in a relational database and allows the incorporation of various geometric representations that best describe the geometry of the object's model. This paradigm can be extended to the representation of FGM objects, where the geometry and composition is defined external to the topological data structure, allowing an accurate modular approach to the design of the FGM modeling system architecture.

The growth of storage cost in the voxelized method is sensitive to the size of the object, and the required geometric and material resolutions. The storage cost of the finite-element mesh approach is a function of the prescribed geometric/material accuracies which depend on the minimum geometric feature size in a bounding surface, maximum geometric curvature of the bounding surface patches, and the minimum intended material feature size and the maximum material curvature within a region. The storage costs of the generalized B-rep data structures are constant with the desired accuracy of representation, and the costs only grow with the number of features present in the model. Figure 4 illustrates a typical growth of the storage cost as the desired geometric/material accuracies vary. Figure 4-(a) shows the storage cost for each representation method with respect to geometric accuracy  $\epsilon_g$  for material accuracy  $\epsilon_m = 10^{-1}$ . A material accuracy  $\epsilon_m = 10^{-1}$  connotes the resolution of 10% in defining the composition. Similarly, Figure 4-(b) is the corresponding result for  $\epsilon_m = 10^{-3}$ . This analysis was performed for a realistic FGM object shown in Figure 3. Memory analysis of the tetrahedral mesh representation was performed for four minor variations of a typical tetrahedral mesh data structure, which results in a group of four graphs in Figure 4. Two kinds of boundary representations (cell-tuple-graph and radial edge) were considered for the analysis of storage cost for the generalized B-rep - (almost identical solid and dashed lines in Figure 4). Each breakpoint (marked by a blue circle) in the graphs for the approximation methods, i.e., voxelized and tetrahedral mesh representations, shows the transition of the storage cost from being a function of geometric accuracy ( $\epsilon_g$ ) to being a function of material accuracy ( $\epsilon_m$ ).

In the course of this project we adopted an FGM object modeler based on (linear) tetrahedral mesh data structure to provide a necessary link to design and process FGM models for fabrication. This choice stems from our observation that the mesh-based FGM data structure is easier to implement than B-rep data structure and in general, less computationally expensive than voxel-based structure - see also Figure 4. The information flow through the mesh-based FGM modeler begins with design of the object shape within a commercial CAD system. Once the geometry of the model is fully defined, it is loaded into a finite-element mesh generator through a neutral file format such as IGES, and meshed into tetrahedra. The composition of the object is established by assigning the composition to the vertices of each tetrahedron. When the composition assignment is complete, the model is sliced at the desired layer thickness and later converted to machine instructions through post-processing steps. The performance of this approach heavily depends on the quality of tetrahedral meshes. One major problem of the currently available tetrahedral mesh generators lies in the difficulty in controlling the local mesh size and shape. Tetrahedral meshing for complicated objects is a complex and memory intensive process, and it may require practically unaffordable processing cost to precisely describe the

intended composition variation within a model. For example, an undesirable fingerprint (marked by a white circle) shown in Figure 5 is caused by the associated tetrahedron that is not fine enough and crosses the medial axis of the model. Similarly, no composition variation within three circular sections in Figure 5 is also resulting from the coarseness of the meshing, i.e., no vertex near the center (degenerate medial axis) of the circle.

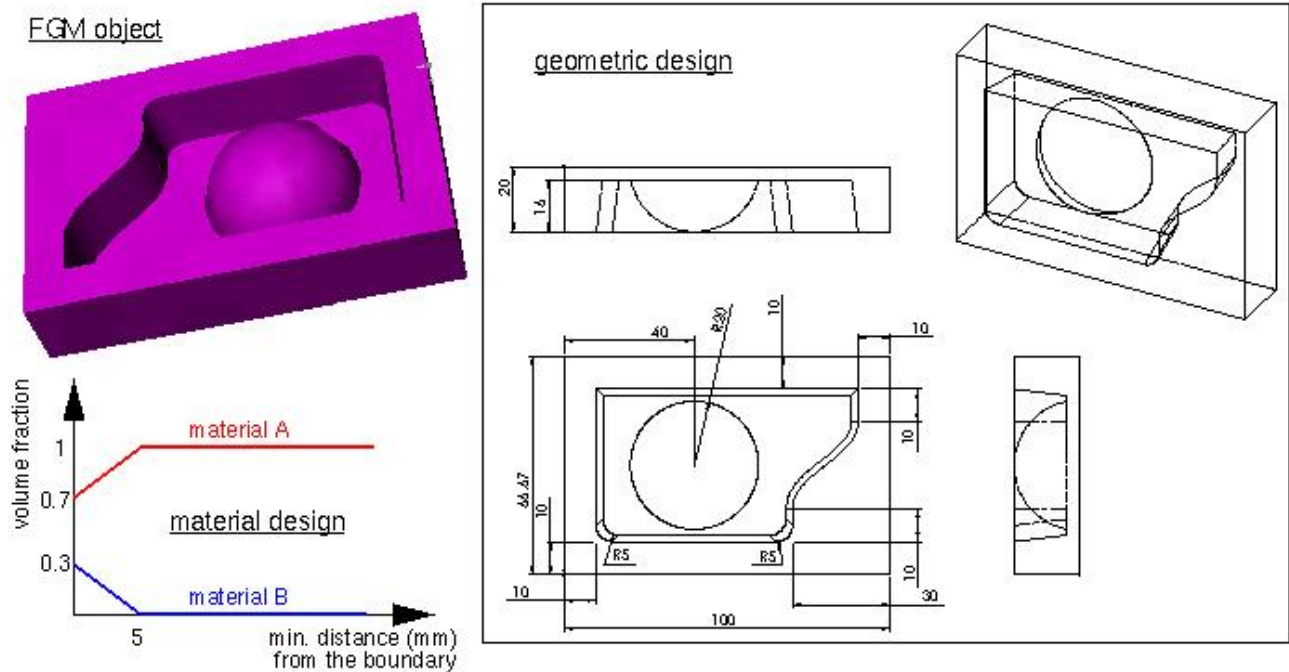


Figure 3: An FGM object: (100mm × 67mm × 20mm) in (fast, slow, vertical) axis, respectively

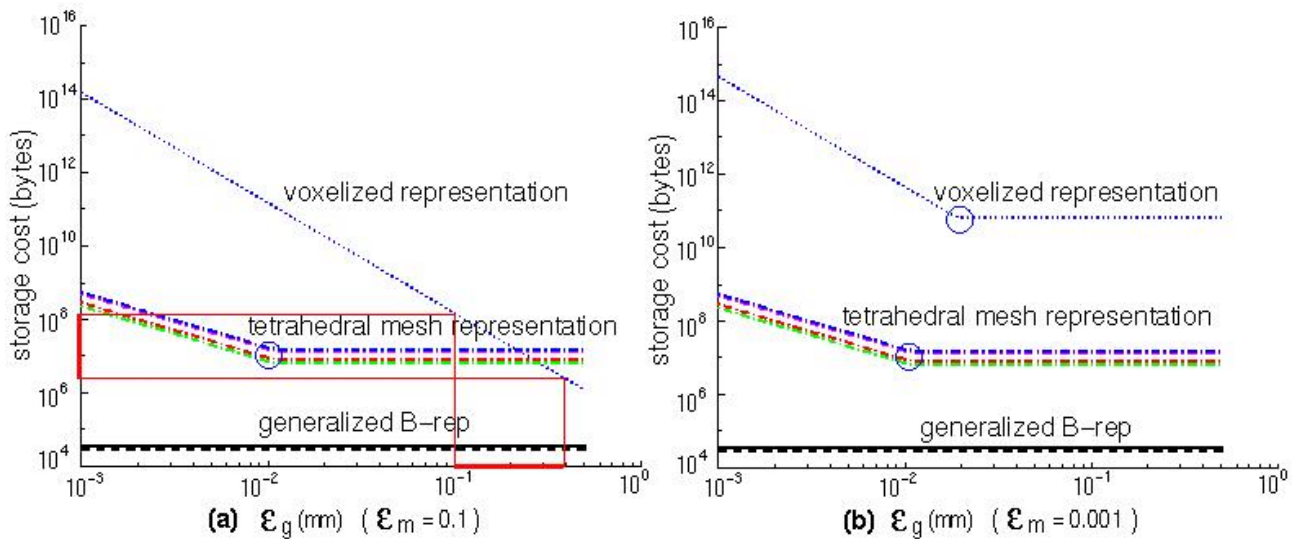


Figure 4: Storage cost w.r.t. geometric resolution ( $\epsilon_g$ ) for material resolutions  $\epsilon_m=10^{-1}$  and  $10^{-3}$

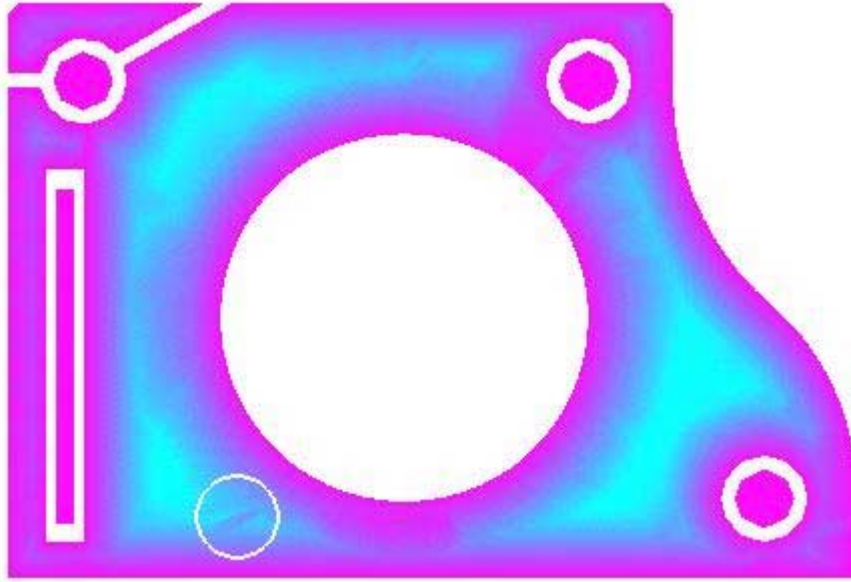


Figure 5: Material slice: linear composition variation w.r.t. the minimum distance from the boundary

Another critical issue involved in the mesh-based approach is the lack of robustness in the tetrahedral mesh generation and the subsequent material slicing processes. This problem is unavoidable as exchanging complicated CAD models are error-prone and the error propagates further in the subsequent complicated meshing/slicing operations mainly due to the imprecise computer arithmetic.

These drawbacks turned our attention to the voxelized modeling scheme, which will serve as link between design and fabrication stages, and is algorithmically simple, robust, and facilitates the control of resolution. As a first step, we need to make sure that the storage cost of the voxelized model falls within a practically affordable cost range for our parameter ( $\epsilon_g$  and  $\epsilon_m$ ) values under consideration. We plan to set a voxel size equal to the size of a three-dimensional dither cell, which actually determines the geometric/material resolution of an FGM object. The size of a 3D dither cell is in fact arbitrary and its composition patterns can be determined by the corresponding 3D threshold matrices. Typically, (4 by 2 by 2) 3D dither cell will be appropriate in (fast, slow, and vertical) axis, respectively. Hence, the associated geometric resolution  $\epsilon_g$  is 0.12mm, 0.404mm, and 0.34mm in each direction, if ( $10\mu m \times 202\mu m \times 170\mu m$ ) PEL is used with a minimum run length 3. For this (4 by 2 by 2) 3D dither cell, its material resolution  $\epsilon_m$  is  $1/(4 \times 2 \times 2) = 0.0625$ . In other words,  $\epsilon_g \in [0.12mm, 0.404mm]$ , and  $\epsilon_m = 0.0625$ . Substitution of this ( $\epsilon_g, \epsilon_m$ ) pair into our storage cost formula in [TRJ00] shows the storage cost for our voxelized model is just a magnification of the result in Figure 4-(a) by a constant scale factor 1.2. For  $\epsilon_g \in [0.12mm, 0.404mm]$  (marked by a red line on the horizontal axis) in Figure 4-(a), the corresponding storage cost is approximately within  $[2 \times 10^6, 10^8]$  (also marked by a red line on the vertical axis). Therefore, rescaling this cost by 1.2 still guarantees the storage cost of our voxelized model is bounded within  $O(10^8)$  bytes. This is an encouraging result. Furthermore, we are currently investigating the efficient distance transform algorithms associated with this voxel-based modeling as described in Section **Design Methods** below.

#### - Pre-Processing:

As an input to our system of design and interrogation of FGM objects, we consider a single solid

represented by a boundary representation obtained from a CAD system, and exchanged via STL, IGES, or STEP file format. The STL data is used for the extraction of geometric boundary information of an imported CAD model. The IGES (or STEP) data is used as an input to tetrahedral mesh generation algorithms. Our data structure is based on the widely-used triangular finite-element meshing structure, and additional attributes such as bucketing system and the association of the facets with their parent subsets of the surface boundary region are included to enhance the efficiency in the evaluation and visualization of a composition.

**- Design Methods:**

We assume that the input geometry is a single solid represented via a boundary representation including tessellated models and curved models, obtained from a CAD system, and exchanged via a standard file format such as STL or STEP. The first algorithm we have already developed allows specification of the FGM composition as a piecewise polynomial or rational function of the minimum distance itself from the entire boundary surface. In order to design FGM composition as a function of minimum distance to the surface of the solids, efficient distance transform is necessary. Among the approaches of distance transform that were presented in the proposal, the space division with rectangular lattice method is particularly useful and easy to implement compared to the methods that involve medial axis transforms or Voronoi diagrams. Specifically, the approach for improving efficiency of distance transform includes preprocessing the model with bucket sorting and digital distance transform of the buckets [HL00-1,HL00-2]. The specific digital distance metric used was chessboard digital distance. Complexity analysis of the algorithm outlined above and experimental results demonstrated effective performance in Figure 6.

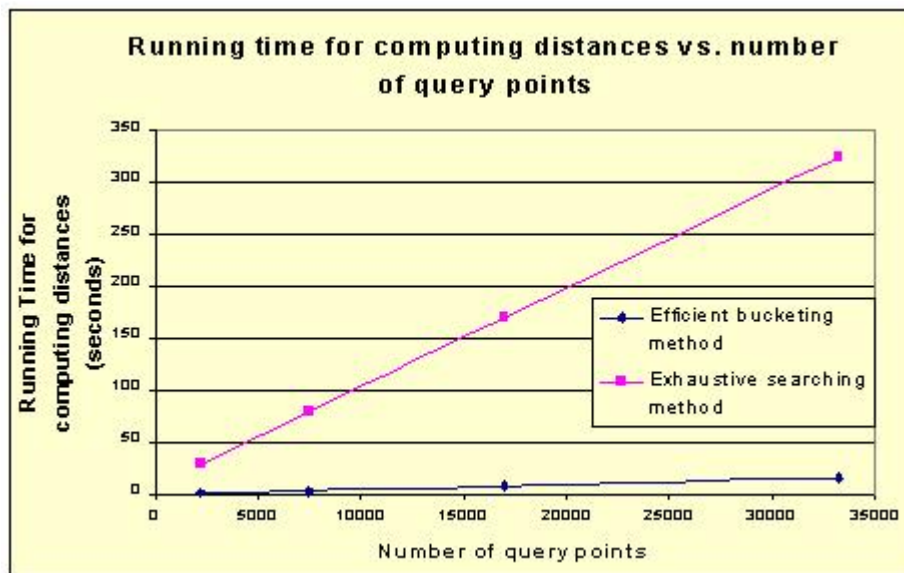


Figure 6: Comparison: time cost of distance computation for an FGM object in Figure 2

When evaluation of the exact Euclidean distance from points within a solid to its boundary can be relaxed, an approximation based on Euclidean digital distance is useful and was investigated. With the model discretized into a large number of subdivisions, the Euclidean digital distance is potentially a

very good approximation of the exact distance. Euclidean digital distance transform (EDT) algorithm developed by Saito & Toriwaki [S-T94] is one of the fastest EDT algorithms, which utilizes certain spatial coherence in scanning direction to improve efficiency.

During the last half of this year, we also plan to develop an algorithm for the specification of FGM composition as a piecewise polynomial or rational function of the minimum distance from the boundary and also varying according to the boundary facet from which the minimum distance is computed from. It is well-known that the distance function from the boundary of a 3D solid is continuous everywhere. It is also differentiable except on the medial surfaces. Once the designer specifies the composition functions for each material (in terms of the minimum distance and also the footpoint), then the problem reduces to developing algorithms for efficient evaluation of composition at either arbitrary points within the solid or a sequence of points that exhibit spatial coherence. The above design methods have possible applications in new turbine blade and heat exchanger designs.

#### - Visualization:

With the composition function evaluated effectively, the visualization of the composition is done through various standard computer graphics techniques. The methods implemented include color-coded point sets, color-coded planar sections, cuberilles, and ray casting of the composition [HL00-2,TRJ00] - see also Figures 5 and 7 for the visualization of a cross section, and a cuberille method, respectively.

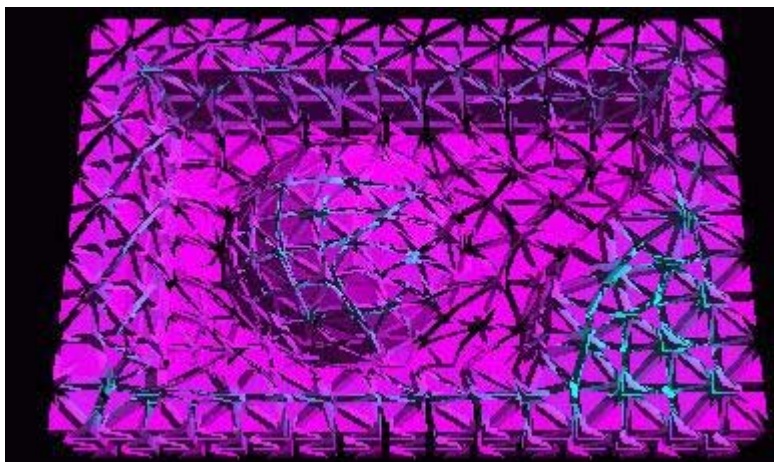
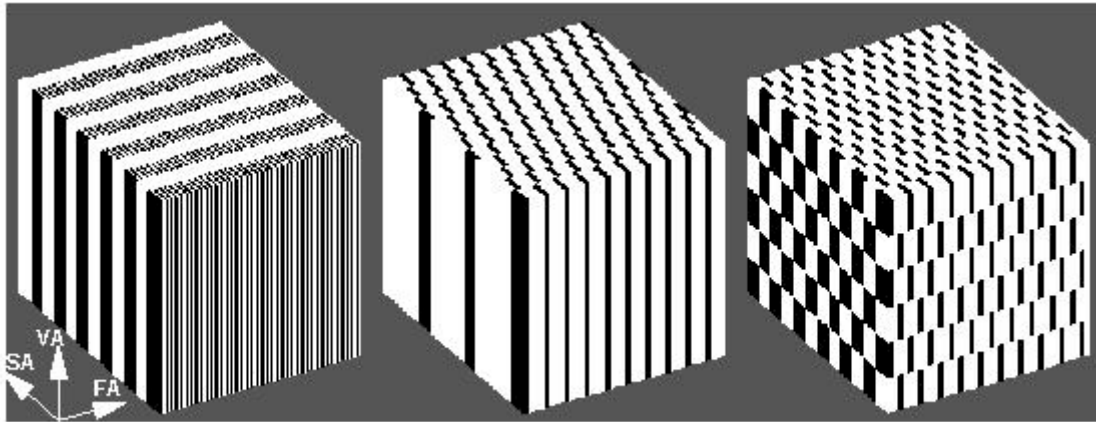


Figure 7: Visualization of a cuberille method for an FGM object in Figure 2

#### - Volume Dithering:

In the information flow for local composition control (LCC) with three-dimensional printing (3DP), a dithering algorithm plays an important role as it converts an idealized continuous-tone FGM representation into discrete version of machine instructions. Motivated by the fact that 3DP process is analogous to ink-jet printing, our dithering algorithm is based on the classical digital halftoning technique [RU87] and adapted to minimize the undesirable low frequency textures of composition not

only layer-wise but over the volume of the FGM model for non-isotropic PEL geometry of 3D printer - see also Figure 8-(c) for the comparison with other dithering approaches in Figures 8-(a,b).



(a) 4 x 4 Bayer's dithering; (b) 4 x 4 2D dithering ( $t = 2$ ); (c) 4 x 4 x 4 volume dithering ( $t = 2$ )

Figure 8: Ditherings within a volume ( $2mm \times 2.4mm \times 2.1mm$ ) of uniform composition (25% black & 75% white)

Compositions over the layers are sampled and compared to a 3D threshold matrices. A binary representation approximating the original, continuous-tone values, is output which is then translated into machine instructions for fabrication.

Due to the physical properties of the fluid as binder and the limits on the speed of the print head, there is a distance between two available binder droplets on the powder bed. For instance, if the frequency of the available droplets is 40KHz and the print head moves at  $1.2m/s$ , the distance between two adjacent droplets is  $30\mu m$ . As the droplet frequency and the print head speed will fluctuate around the pre-defined values with a small variation, it is hard to determine the precise location of the droplet inside the  $30\mu m$ -wide region. Considering the hardware resolution (i.e., the width of a PEL) of the 3D printer is  $10\mu m$ , we need to grant the three PELs in the  $30\mu m$ -wide region identical value. This is called minimum run length ( $l$ ) requirement, and handled in the dithering process by using a dither PEL of width ( $l \times$  hardware resolution).

Volume dithering algorithm also takes into account technical limitations in the machine, only generating lattices that can be represented within the memory limits of the current hardware implementation in the 3D Printer. For example, current 3DP machine has provisions for loading eight different patterns for each nozzle. Considering the feature of dithering patterns<sup>2</sup>, the limitation in the available machine patterns restricts the number of dither PELs to eight, only in the direction of fast axis, while we can still achieve as high a material resolution as possible by controlling the size of dither cell along the other directions.

<sup>2</sup> Once a dot is added into a dither cell, it will never be removed or moved to another location as the material density increases.

### Encoding:

The encoding is composed of three main steps, i.e., rastering the geometric slice, generating a state

map of the pixels for each material, and encoding the state map into printing instructions.

The raster of the geometric slice is an analogy to the technique used in displaying a filled polygon on a CRT screen. Since the electronic gun of a CRT monitor draws only one line at a time, to display a filled polygon it needs to draw several raster lines. In one raster line, it starts lighting the pixels at the boundary of the polygon and stops lighting the pixels at the next boundary it meets and then iterates. In 3D Printing, we also need to generate these raster segments for each nozzle. Rather than lighting a pixel, the nozzle prints a droplet inside the raster segment.

With the raster segments generated, we then match each segment with the halftone result of the material. This will further break the raster segment into several shorter segments, namely Materialized Raster Segment (MRS). Each MRS covers the consecutive dither-cell rows with identical Dither-cell-row Pattern. Each dither cell is composed of several rows. Each row has a determined state or pattern as of the states of all the PELs in this row (filled or not) for a given composition. This pattern is called a Dither-cell-row Pattern. Two adjacent dither cells in the halftone result may have different composition values, but they may have the same Dither-cell-row Pattern for a certain row. In this case, that row in the two dither cells will be put into the same MRS. After processing all raster segments on one material, we actually obtain a run-length representation of a state map of all the pixels for this material in a layer. As a result, we now have a state map for each material on each layer.

Next, we encode the MRS's into machine instructions based on the pattern capability of the 3D Printing machine, i.e.,  $\alpha$ -machine at MIT. It is quite straightforward to transform a Dither-cell-row Pattern into a nozzle pattern. An issue in this step is to allocate nozzles to different materials. Due to the property of the printhead on the  $\alpha$ -machine, the nozzles have to be allocated in a pair-wise manner. If we have four materials, for instance, we will allocate nozzles 0 and 1 to material A, nozzles 2 to 3 to material B, etc. If we only have three materials, then nozzles 6 and 7 will be idle. No printing instruction will be generated for these nozzles. Since there are only 8 nozzles on  $\alpha$ -machine, this imposes another limitation on the number of material we can have. For  $\alpha$ -machine, at most four materials can be printed at the same time.

After allocating nozzles to material, a map from the nozzle index to the state map that should be used when generating the instructions is established. Then the software simply determines at a given printing time what part of the state map each nozzle should use and generate proper instructions from it.

At this stage, an instruction file is generated and output in a binary format that can be interpreted by the controlling software on the  $\alpha$ -machine. The controlling software then writes the instructions into the controlling card, which will drive the printing machine eventually.

### - 3D Printing:

3D Printing of parts with local composition control is being accomplished on the MIT  $\alpha$ -machine. The primary characteristic of this machine is that it has an 8-jet continuous-jet printhead, which defines the part by raster scanning over the powderbed. Continuous-jet printing is the preferred technology for accomplishing local composition control, because it allows for the widest range of options in binder materials to be printed. Continuous-jet printing has demonstrated the capacity to print aqueous and solvent-based materials, colloids and slurries, and dissolved matter. The one negative factor associated

with the use of continuous-jet printing for local composition control is that with the current technology, there is an uncertainty of 1 droplet in any run length. In other words, if we ask for 2 sequential droplets of material A, we may get as many as 3 or as few as 1. This factor has been accommodated by developing dithering algorithms, which allow us to specify minimum run lengths (see Section **Volume Dithering** above). It should be noted that in desktop ink-jet printers, color printing is accomplished with drop-on-demand type printheads. While these printheads do allow for the accurate specification of run length, including printing single droplets, they do not allow for the use of a wide range of materials.

The 8-jet printhead on the  $\alpha$ -machine was configured with two banks of 4 jets each. Special manifolds and fluid recirculation components were fabricated to keep the two fluids isolated. For demonstration purposes, printing was accomplished using colored inks, cyan and magenta, on a white alumina ceramic powder, so that the colors would show up well. In this case, the binder carried color only, and a dissolvable, polymeric powder (poly-vinyl alcohol: PVA) was added to the powder. Thus, when the aqueous dye hits the powder, it locally dissolves some of the PVA in order to bind the part, while the printed dye imparts the color.

The  $\alpha$ -machine has the capability to store the definition of 8 patterns for each of the jets. As explained above, the halftoning algorithms are designed so that in any given pass of the printhead, only 8 patterns will be required. However, the full definition of the image requires more than 8 patterns, and so at the beginning of each pass, some of the patterns must be overwritten in the pattern memory for each nozzle. At the present time, this pattern writing slows the process down considerably, resulting in a total time to print each layer of approximately 5 minutes (contrast this with less than 1 minute for single material printing). Future systems with more pattern memory can, of course, greatly increase printing speed.

#### - References:

[RU87] "Digital Halftoning" by R. Ulichney. MIT Press, Cambridge, MA, 1987.

[S-T94] "New Algorithms for Euclidean Distance Transformation of an N-Dimensional Digitized Picture with Applications" by T. Saito and J. Toriwaki, Pattern Recognition, Vol. 27, No. 11 pp 1551-1565, 1994. Elsevier Science Ltd.

#### - Publications:

[CHO-00] "Methods for Distributed Design and Fabrication of Parts with Local Composition Control" by W. Cho, E. M. Sachs, N. M. Patrikalakis, H. Liu, H. Wu, T. R. Jackson, C. C. Stratton, J. Serdy, M. J. Cima, and R. Resnick. To appear in the Proceedings of the 2001 NSF Design and Manufacturing Grantees Conference, Tampa, FL, USA, January 2001.

[HL00-1] "[Algorithms for Design and Interrogation of Functionally Gradient Material Objects](#)" by H. Liu, W. Cho, T. R. Jackson, N. M. Patrikalakis, and E. M. Sachs. Proceedings of ASME 2000 IDETC/CIE, 2000 ASME Design Automation Conference, September 10-13, 2000, Baltimore, Maryland, USA.

[HLOO-2] "[Algorithms for Design and Interrogation of Functionally Graded Material Solids](#)" by H. Liu, Master's thesis, Massachusetts Institute of Technology, February 2000.

[TRJ00] "Analysis of Functionally Graded Material Object Representation Methods" by T. R. Jackson, PhD thesis, Massachusetts Institute of Technology, January 2000.

[HW00] "Distributed Design and Fabrication of Parts with Local Composition Control" by H. Wu, E. M. Sachs, N. M. Patrikalakis, D. Brancazio, J. Serdy, T. R. Jackson, W. Cho, T. R. Jackson, H. Liu, M. Cima, and R. Resnick. Proceedings of the 2000 NSF Design and Manufacturing Grantees Conference.

[EMS99] "The Distributed Design and Fabrication of Metal Parts and Tooling by 3D Printing" by E. M. Sachs, N. M. Patrikalakis, M. J. Cima, D. Brancazio, W. Cho, T. R. Jackson, H. Liu, H. Wu and R. Resnick. Proceedings of the 1999 NSF Design and Manufacturing Grantees Conference. Long Beach, California, January 1999.

[TRJ98] "Modeling and Designing Components with Locally Controlled Composition" by T. R. Jackson, N. M. Patrikalakis, E. M. Sachs, M. J. Cima. Proceedings of the 1998 Solid Freeform Fabrication Symposium, The University of Texas at Austin, Austin, Texas, 1998.

[EMS98] "The Distributed Design and Fabrication of Metal Parts and Tooling by 3D Printing" by E. M. Sachs, N. M. Patrikalakis, D. Boning, M. Cima, T. Jackson and R. Resnick. Proceedings of the 1998 NSF Design and Manufacturing Grantees Conference. Monterrey, Mexico. January 1998. pp. 35-36. Arlington, VA: NSF, 1998.

---

### **Participation on Other Research Projects.**

PIs also participate in NSF project (DMII): "The Distributed Design and Fabrication of Metal Parts and Tooling by 3D Printing", closely related to this project.

---

### **Transitions and DOD Interactions.**

In March 2000, we have held a 3DP Consortium meeting, which several companies (ExtrudeHone, Soligen, TDK Corporation, Specific Surface Corporation, Therics, and Z Corporation) and government sponsors (from NSF, NRL, DARPA) attended. Another such 3DP Consortium meeting is scheduled for later in September, 2000.

---

### **Software and Hardware Prototypes.**

1. Prototype Name: 3DP application

+ URL: <http://www.mit.edu/~tdp>

+ Availability: Prototype phase (upgraded from yr. 1999's version), for evaluation within MIT

+ Description: A Windows-based application developed in the Three Dimensional Printing Laboratory and Design Laboratory at MIT. It offers a tool for a complete information pathway for FGM object design, interrogation, and its fabrication through 3D printing. This year, the application is upgraded for the fabrication of functionally graded multi-material solids.

---

**Honors, Prizes, Awards, or Promotions Received.**

None.

---

**Current Students and Recent Graduates Supported by ONR.**

None.

---

**Sabbatical Plans.**

None.

---

**Related Research Projects.**

NSF DMII has funded related work on SFF at MIT.

---